ACS Photonics

Letter

Cite This: ACS Photonics 2019, 6, 3082−3091

pubs.acs.org/journal/apchd5

Twisted-Angle-Dependent Optical Behaviors of Intralayer Excitons and Trions in WS_2/WSe_2 Heterostructure

Jia Shi,[†,#] Yuanzheng Li,[†,‡,#] Zhepeng Zhang,[§,∥,#] Weiqiang Feng,[⊥] Qi Wang,[†] Shuliang Ren,[○,△] Jun Zhang,[○,△] Wenna Du,[†,□] Xianxin Wu,[†,‡] Xinyu Sui,[†,‡] Yang Mi,[†] Rui Wang,[†] Yuanhui Sun,[○] Lijun Zhang,[○] Xiaohui Qiu,[†] Jiong Lu,[▽] Chao Shen,[*,○,△] Yanfeng Zhang,[∥,⊥] Qing Zhang,[*,∥] and Xinfeng Liu[*,†]

[†]CAS Key Laboratory of Standardization and Measurement for Nanotechnology, CAS Center for Excellence in Nanoscience, National Center for Nanoscience and Technology, Beijing 100190, China

[‡]Centre for Advanced Optoelectronic Functional Materials Research and Key Laboratory of UV-Emitting Materials and Technology, Northeast Normal University, Ministry of Education, Changchun 130024, China

[§]Department of Materials Science and Engineering, College of Engineering, Peking University, Beijing 100871, China

[∥]Academy for Advanced Interdisciplinary Studies, Peking University, Beijing 100871, China

[⊥]Key Laboratory of Automobile Materials of MOE, State Key Laboratory of Superhard Materials, and College of Materials Science and Engineering, Jilin University, Changchun 130012, China

[○]College of Materials Science and Optoelectronic Technology, University of Chinese Academy of Science, Beijing 100049, China

[△]State Key Laboratory of Superlattices and Microstructures, Institute of Semiconductors, Chinese Academy of Sciences, Beijing 100083, China

[□]Key Laboratory of Semiconductor Materials Science, Beijing Key Laboratory of Low Dimensional Semiconductor Materials and Devices, Institute of Semiconductors, Chinese Academy of Sciences, Beijing, 100083, China

[▽]Department of Chemistry Faculty of Science, National University of Singapore, 119077, Singapore

Supporting Information

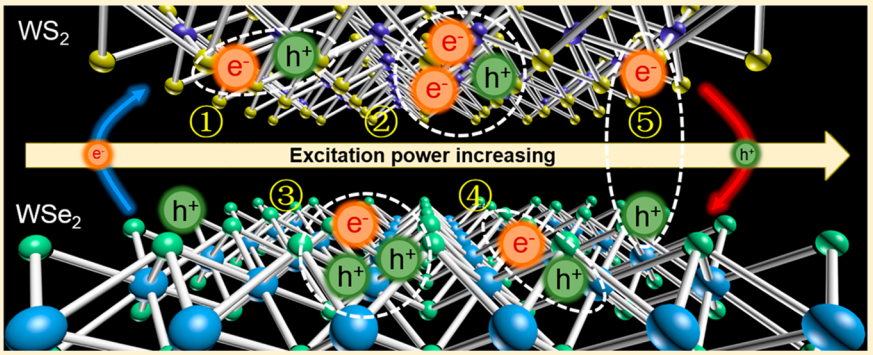

ABSTRACT: Understanding the formation and recombination dynamics between excitons and trions is critical for evaluating and improving the performance of two-dimensional material-based optoelectronic devices. Herein, we have investigated the competitive luminescence processes of intralayer excitons and trions in WS_2/WSe_2 heterostructures with different (0°, 30°, and 60°) twisted angles. We observed the increased photoluminescence (PL) ratio of trions compared to excitons in heterostructures with twisted angles of 30° and 60°. For a twisted angle of 30°, the relatively large PL ratio of trions is caused by the high probability of trion formation than that of excitons, while for a twisted angle of 60°, the ultrafast formation time of trions is the main reason for the trion-dominant proportion in the PL spectrum. Moreover, the power law between the excitation laser and the PL emission intensity reflects how the many-body effect affects the competition luminescence of excitons and trions. Our present results provide further understanding of the optical behaviors of intralayer excitons and trions in different twisted angle heterostructures.

KEYWORDS: *WS_2/WSe_2 heterostructure, twisted angle, excitons, trions, carrier dynamics*

Engineering Coulomb interactions between layers give rise to novel physical phenomena and designable optoelectronic devices in van der Waals (vdW) heterostructures.[1−3]

Received: June 12, 2019
Published: November 15, 2019

DOI: 10.1021/acsphotonics.9b00855
ACS Photonics 2019, 6, 3082−3091

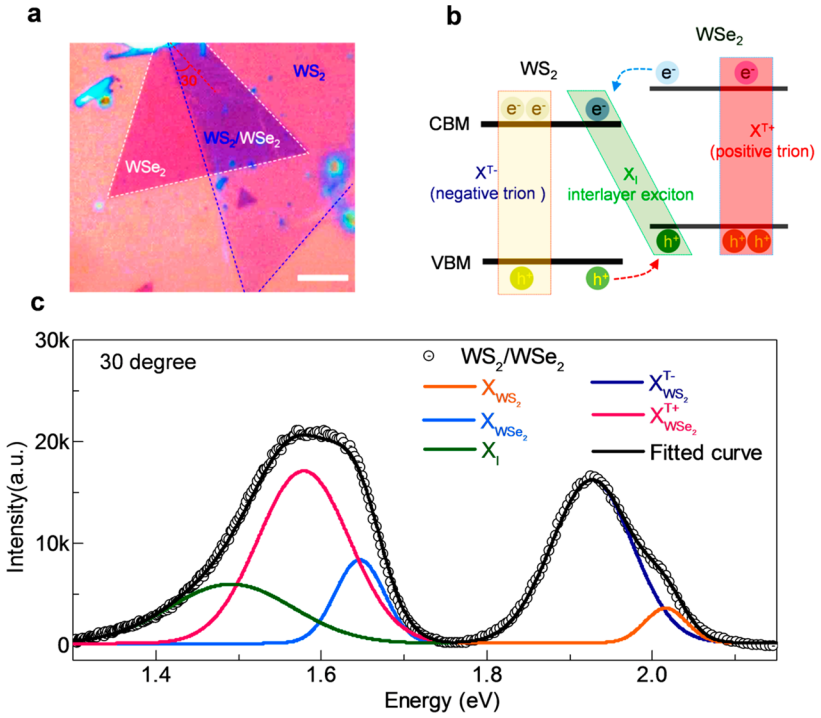

Figure 1. (a) One typical optical image of a WS_2/WSe_2 heterostructure with a twisted angle of 30°. The scale bar is 10 μm. (b) Schematic view of the formation of a negative trion (X^{T-}) in WS_2, a positive trion (X^{T+}) in WSe_2, and an interlayer exciton (X_I) between layers. The blue dashed arrow and red dashed arrow show schematically the electrons and holes transferred between WS_2 and WSe_2. (c) PL spectra measured at the WS_2/WSe_2 heterostructure with twisted angle of 30°.

Two types of Coulomb interaction are mainly included in vdW heterostructure: intralayer and interlayer. The intralayer Coulomb interaction in an atomically thin layer is poorly screened, which leads to the formation of intralayer excitons (so-called neutral excitons) with high binding energy of hundreds of millielectronvolts.[4−7] However, in the presence of residual free electrons or holes, excitons interact with excess electrons or holes and bind to each other to form charged positive or negative trions.[4,5] For the interlayer Coulomb interaction, the separation of electrons and holes between adjacent layers leads to the emergence of interlayer excitons with lifetimes of several nanoseconds.[6] These "many-body" species are elementary quasi-particles, and Coulomb interactions between them are of vital importance as they are the key parameter that determine the nature of the electronic properties of the material for quantum information,[7] valleytronics devices,[8−10] and coherent control applications.[11,12] "Many-body effect" will affect the electronic properties (the carrier mobility, device performance) and arise in linear and nonlinear optical spectroscopy of semiconductors. Many aspects of the optical response of semiconductors can be described successfully by microscopic many-body theory. Already in the linear optical regime the Coulomb interaction leads to characteristic signatures, that is, the so-called excitonic effects, which are a consequence of the Coulomb attraction between photoexcited electrons and holes. Here we focus on the excitonics and trionic effects in the heterostructure with different twisted angles.

Manipulating the Coulomb interaction of intralayer excitons and trions in two-dimensional materials has been employed by various means, such as electrical control,[13,14] dielectric screening,[15,16] and chemical doping.[17,18] However, momentum mismatch and the regulation of the Coulomb interaction induced by twisted angles between layers have a relatively large impact on the emergence of interlayer excitons, the transition rate, and the binding energy and valley lifetime of intralayer excitons,[6,19−24] giving rise to a variety of fascinating physical behaviors (e.g., Hofstadter's butterfly and an interlayer moiré potential[25−28]). Research on controlling the relative twisted angles of the heterostructure is still needed; however, the appearance of these novel physical phenomena requires extremely high sample quality and ultralow temperature, which further limits the application of the heterostructure in practical optoelectronic devices. Meanwhile, intralayer excitons and trions with different Coulomb interactions between two layers are governed by different twisted angles.[29] As a result, interlayer excitons and intralayer trions induced by charge transfer in a twisted vdW heterostructure are always accompanied by complicated electron−hole, electron−hole−electron, or electron−hole−hole relaxation pathways. All these limitations hinder a clear understanding of the physical behavior of excitons or trions in the twisted angle heterostructure for further application in fields such as controllable valleytronics or quantum information devices.

In this work, we have investigated twisted-angle-dependent optical behaviors of intralayer excitons and trions in the WS_2/WSe_2 heterostructure at room temperature. From steady-state photoluminescence (PL) spectra, the increased luminescence ratio of trions in the heterostructures with twisted angles of 30° and 60° were observed. To understand the PL features tuned by the different twisted angles, ultrafast transient absorption spectra were used to directly monitor the fomation rates of excitons and trions and the hole concentrations were calculated according to the mass action model. The formation time for trions being much faster than that of intralayer excitons, thus, making the luminescence of trions stronger in

DOI: 10.1021/acsphotonics.9b00855
ACS Photonics 2019, 6, 3082−3091

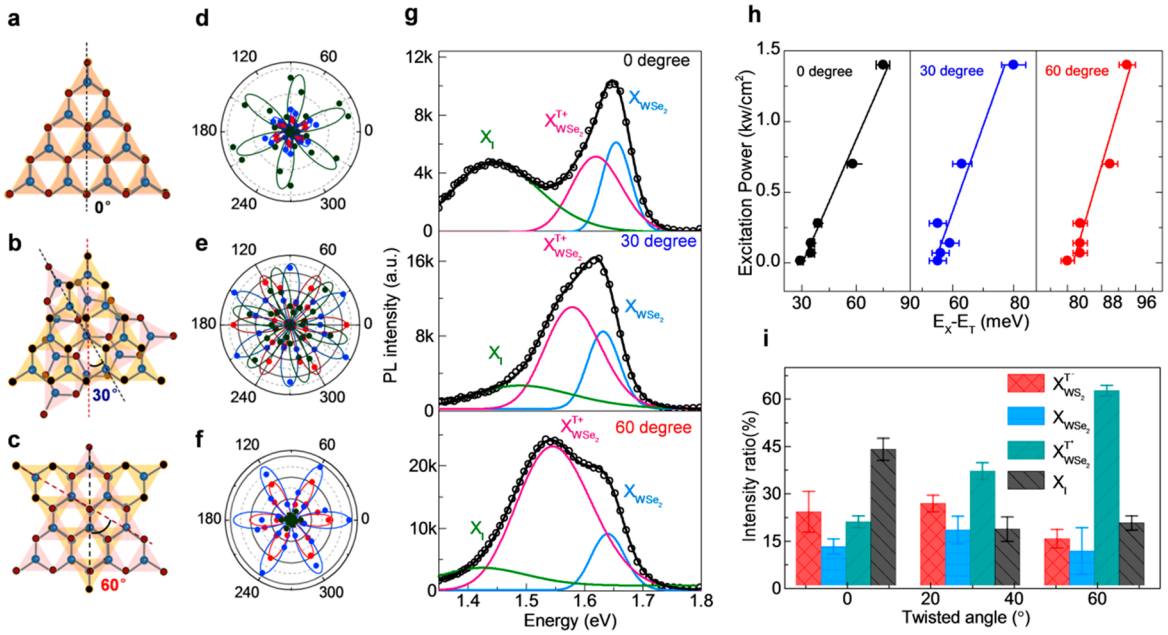

Figure 2. (a–c) Top view of the atomic structures of the WS_2/WSe_2 heterostructure with different twisted angles (0°, 30°, and 60°, respectively). The top layer is monolayer WS_2, represented by orange triangles; smaller symbols represent S atoms. The bottom layer is monolayer WSe_2, represented by pink triangles; smaller symbols represent Se atoms. The black and red dashed lines correspond to orientations of WS_2 and WSe_2, respectively. (d–f) Angle dependence of SHG intensity for the WS_2/WSe_2 heterostructure with different twisted angles (0°, 30°, and 60°, respectively). (g) PL spectra of the WS_2/WSe_2 heterostructure with twisted angles of 0°, 30°, and 60°, respectively. The spectral bands are fitted by a Gaussian function to the observed spectral shapes. (h) Power-dependent peak position (X^{T+} and X_{WSe_2}) and binding energy of the positive trions of the WS_2/WSe_2 heterostructure. (i) Histogram of the peak intensity ratio distributions of the WS_2/WSe_2 heterostructure with twisted angles of 0°, 30°, and 60°, respectively, extracted in (g).

the 60° twisted heterostructure. The photogenerated carriers were quickly separated owing to the potential energy gradient, which then led to the accumulation of a large number of residual carriers in the monolayer, resulting in a higher probability of trion formation than that of exciton in the heterostructure with a twisted angle of 30°. All these results provide us with a further understanding of the competition mechanism of intralayer excitons and trions in heterostructures with different twisted angles.

RESULTS AND DISCUSSION

Single-layer WS_2 (P type) and WSe_2 (N type) were grown by chemical vapor deposition (CVD) and then transferred on 285 nm SiO_2/Si substrates to form a type II WS_2/WSe_2 heterostructure with different twisted angles. Figure 1a shows an optical image of the typical WS_2/WSe_2 heterostructure with a twisted angle of 30°. The schematic view in Figure 1b indicates the formation mechanism of negative charged trions (electron–electron–hole) in WS_2, positive charged trions (electron–hole–hole) in WSe_2, and interlayer excitons between two adjacent layers (the intralayer excitons are not shown here). In Figures 1c and S1a and b, the typical PL spectra of WS_2/WSe_2, monolayer WSe_2, and monolayer WS_2 are exhibited, respectively. The PL spectra of monolayer WS_2 and monolayer WSe_2 can be fitted by two Gaussian peaks, which are associated with intralayer excitons (X_{WSe_2} and X_{WS_2}) and charged trions ($X^{T+}_{WSe_2}$ and $X^{T-}_{WS_2}$), respectively. The power-dependent PL spectrum of monolayer WSe_2 is constructed to further determine whether the source of the peak-fitting component is reliable, as shown in Figure S1c. As previously reported, intralayer excitons and trions in transition-metal dichalcogenides (TDMCs) materials exhibit a linear dependence as a function of power.[30,31] In our experiment, the peak intensities of X_{WSe_2} and $X_{WSe_2}^{T+}$ and excitation powers both satisfied a linear relationship with a slope close to 1 (Figures S1d). In the heterostructure region, these peaks are largely suppressed, and they can be assigned to the charge separation between the adjacent WS_2 and WSe_2 as a result of the formation of a type II heterostructure. In terms of PL intensity, recombination of intralayer excitons dominates the PL spectra for the monolayer region, whereas, for the heterostructure region, the recombination of trions plays an important role in the PL emission spectra.

To determine the twisted angle of the WS_2/WSe_2 heterostructure, we identified the orientation of the monolayer by using angle dependent second harmonic generation (SHG) spectra. Monolayers WS_2 and WSe_2 both exhibit a 6-fold symmetric response as a function of rotation angles.[32−35] As previously reported,[36] SHG intensities of both WS_2 and WSe_2 satisfy the expression $I_{SHG} = I_0 \cos^2(3\theta)$, where θ indicates the angle between the armchair direction and the polarization of the pump beam. If the input pump beam has the same polarization with the armchair direction of monolayer, the SHG intensity reaches its maximum value of I_0. In our work, both SHG intensity and twisted angle were obtained, which made angle-dependent SHG measurements a common method for determining twisted angles without destroying the sample. The atomic structure diagrams of stacking order of WS_2/WSe_2 heterostructure with different twisted angles are displayed in Figure 2a–c. The top layer is monolayer WS_2, represented by orange triangles; the smaller symbols represent S atoms. The bottom layer is monolayer WSe_2, represented by pink triangles; the smaller symbols represent Se atoms. The black and red

DOI: 10.1021/acsphotonics.9b00855
ACS Photonics 2019, 6, 3082−3091

dashed lines correspond to orientations of WS_2 and WSe_2, respectively. In contrast to natural bilayers (Bernal stacking order) that generate zero SHG signal, the SHG of the heterostructure is the stacking angle that is dependent and consistent with the twisted angles measured above. More interesting is that the intensity and orientation of the heterostructure with different twisted angles exhibit distinct behaviors owing to the artificial stacking orders induced by symmetry breaking. As shown in Figure 2d−f, the red, blue, and green dots are consistent with the angle-dependent SHG intensity of the monolayer WS_2, monolayer WSe_2, and the heterostructure, respectively. The twisted angles between monolayer WS_2 and monolayer WSe_2 extracted from Figure 2d−f are determined to be 0°, 30°, and 60°, respectively. For a heterostructure with a twisted angle of 0° (see Figure 2a), the orientations of WS_2 and WSe_2 are arranged in the same direction that makes the atomic structure satisfy the broken inversion symmetry. As a result, the SHG intensity of WS_2/WSe_2 is significantly enhanced compared to that of monolayer WS_2 or monolayer WSe_2, and the heterostructure maintains a 6-fold symmetry, with the orientation parallel to that of both top and bottom layers. When the twisted angle is 30°, the atomic structures maintain a broken inversion symmetry, which yields the same SHG intensity as that of monolayer WS_2 or monolayer WSe_2. Besides, the heterostructure orientations are in the direction in which the angle between WS_2/WSe_2 and WS_2 or WSe_2 is 15°. In terms of the twisted angle of 60°, the resultant atomic structures show relatively good in-plane symmetry. Fortunately, the different S atoms and Se atoms provided by the top and bottom layers lead to broken inversion symmetry and yield a weak SHG intensity, as shown in Figure S2.

After determining the twisted angles, we conducted a steady-state PL experiment of heterostructure with different angles and systematically analyzed the competitive luminescence processes of intralayer excitons, trions, and interlayer excitons. The corresponding angle-dependent PL spectra are shown in Figure 2g; the excitation energy was fixed at 2.41 eV, which is above the band gap value of WS_2 and WSe_2 to ensure that both materials can be excited. As can be seen from the PL spectra, the negative trions $X_{WS_2}^{T-}$ account for the dominant PL intensity of WS_2, which means there is a high enough concentration of electrons transferred from WSe_2 to WS_2. The intralayer excitons X_{WSe_2}, positive trions $X_{WSe_2}^{T+}$, and interlayer excitons X_I share different proportions for different heterostructure twisted angles owing to the distinct Coulomb interaction between them. Obviously, X_I of the 0° stacked heterostructure exhibits a PL intensity comparable with that of other peaks, which indicates that large proportions of electrons and holes are separated in WS_2 and WSe_2 layers in this case. For the heterostructure with a twisted angle of 30°, the PL intensity of $X_{WSe_2}^{T+}$ exhibits a growth trend and X_I occupies only a very small fraction of the PL intensity. Intriguingly, $X_{WSe_2}^{T+}$ accounts for the majority of the PL intensity in the 60° stacked heterostructure, and X_I and X_{WSe_2} play only minor roles in the PL spectrum. Moreover, the position of intralayer and interlayer excitons in the heterostructure with different twisted angles exhibits a slight shift compared to others. This phenomenon can be well explained by the different band structures of heterostructures caused by different stacking configurations, as calculated by using density functional theory (DFT) and shown in Figure S3a−c. According to the results of the peak fitting of PL spectra, we have determined the peak position of trions of WSe_2 and calculated the corresponding binding energies of trions to be ∼31, 52, and 80 meV for heterostructures with twisted angles of 0°, 30°, and 60°, respectively. The binding energy of trions based on the peak difference between intralayer excitons and trions versus excitation power is plotted in Figure 2h (more details in Figures S4 and S5). The trion binding energy is obtained by formula $E_b = E_X - E_T$, where the E_X and E_T are the exciton and trion peak energy of the WSe_2 monolayer, respectively.[14,37,38] We also calculated the ratio of each peak in the heterostructure with different twisted angles and plotted a histogram of the peak intensity ratio as a function of twisted angle extracted from Figure 2g in Figure 2i. For the heterostructure with a twisted angle of 0°, the peak intensity ratio of interlayer excitons reaches 43%, which indicates the effective electron and hole separation between WS_2 and WSe_2 layers. In terms of the heterostructure with a twisted angle of 30°, positively charged trions of WSe_2 and negative charged trions of WS_2 occupy a relatively large part of the PL emission. The ratio of interlayer excitons exhibits an apparent reduction, which probably originates from the mismatch of momentum between WS_2 and WSe_2. For the heterostructure with a twisted angle of 60°, the ratio of $X_{WSe_2}^{T+}$ exhibits predominance with a value of 62%. The interlayer excitons PL ratio in 60° stacked heterostruture is larger than that of 30°, but smaller than that of 0° stacked heterostructure. The larger interlayer PL ratio in a 0° and 60° stacked heterostructure is caused by its stronger interlayer coupling and momentum matching as proved by the low-frequency (LF) Raman spectra in Figure S6. However, not only the momentum matching and stronger interlayer coupling give rise to a higher formation probability for interlayer excitons, but also the charge transfer induced intralayer trions will compete with the interlayer excitons and affect PL emission of interlayer excitons from K valley. The reason why the PL emission ratios of interlayer excitons in 0° and 60° stacked heterostructure are different will be discussed in the following section.

Moreover, to exclude the different optical behaviors from sample-to-sample variations induced by the transfer process, we also carried out several groups of heterostructure with other twisted angles and corresponding statistical histogram of different proportion of X_{WSe_2}, $X_{WSe_2}^{T+}$, and X_I as a function of twisted angle in WS_2/WSe_2 heterostructure, as shown in Figure S7. They exhibit similar PL spectra of Figure 2g and confirmed the authenticity of the data. Besides, based on the statistical analysis of the angle-dependent distribution of peak position and peak ratio for quasi-particles, the heterostructures with other twisted angles exhibited a similar optical behavior with selected representative heterostructures with twisted angles of 0°, 30°, and 60°. To predict the optical behaviors of random twisted heterostructures, we can assign the twisted angle to their close one. If it is close to 0°, interlayer excitons occupy a favorable competitive position in luminescence due to momentum matching. If the twisted angle is close to 30°, a large number of carriers are accumulated in the single layer material due to the momentum mismatch, resulting in an increased formation probability of trions. However, if the twisted angle of the heterostructure is close to 60°, due to its special stacking sequence, the binding energy of the trions becomes larger, which makes the formation of trions much

DOI: 10.1021/acsphotonics.9b00855
ACS Photonics 2019, 6, 3082−3091

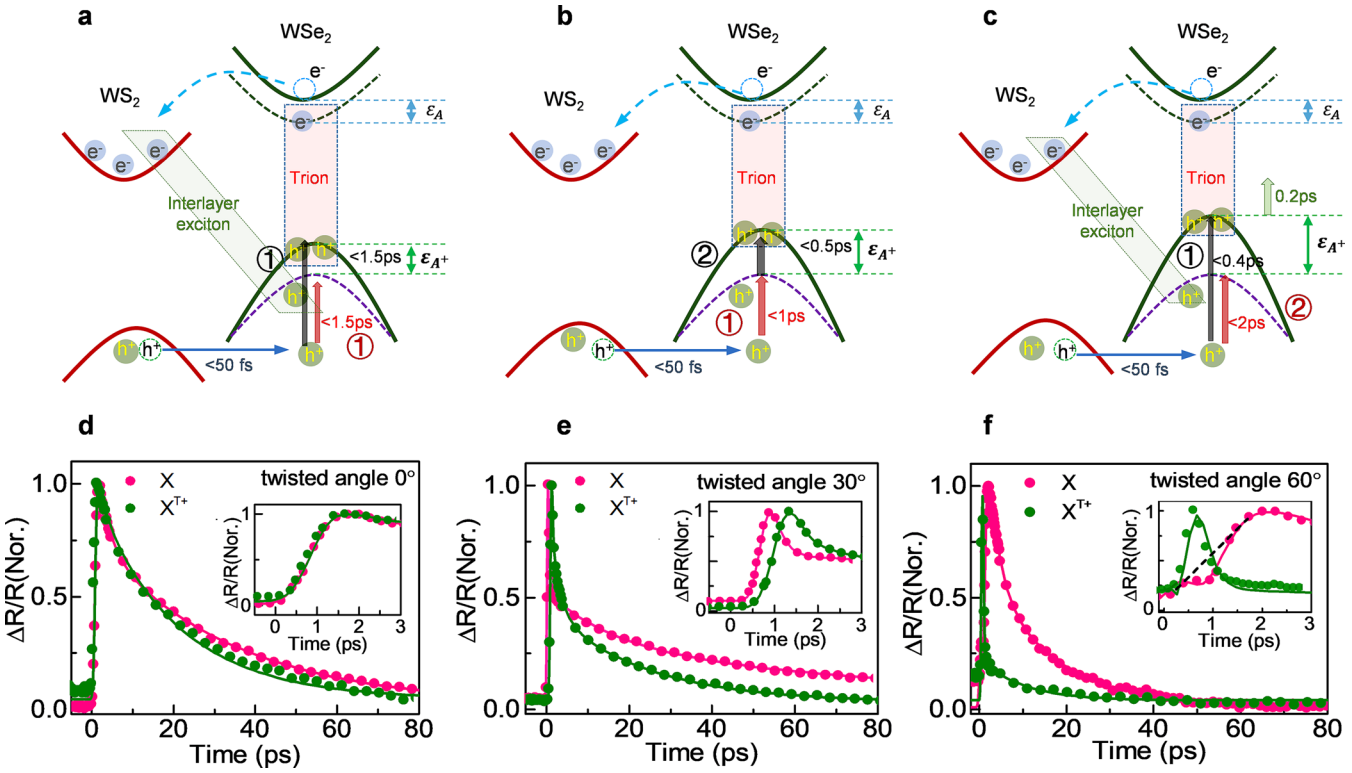

Figure 3. (a–c) Schematics of exciton- and trion-related radiative transitions between the WS_2 and WSe_2 valleys at the *K* point in the Brillouin zone. ε_A and ε_A^+ represent the binding energies of neutral excitons and positive trions, respectively. (d–f) Differential reflection signal measured from the WS_2/WSe_2 heterostructure with twisted angles of 0°, 30°, and 60°, respectively. The pink and green solid lines indicate biexponential or triexponential decay fits of neutral excitons and trions, respectively. The inset of (d–f) is a plot of the corresponding differential reflection signal on a short time scale within 3 ps.

easier and the PL emission of trions takes a favorable proportion.

Moreover, we measured the low temperature (77 K) PL spectra of the heterostructure with twisted angles of 0°, 30°, and 60° to further confirm the assignment of PL peak fitting results in Figure 2g. The corresponding PL spectra ranging from room temperature to liquid nitrogen temperature (77 K) of heterostructures with twisted angles of 0°, 30°, and 60° are shown in Figure S8. As can be seen from Figure S8a, as the temperature decreases, the proportion of luminescence of interlayer excitons increases significantly in 0° stacked heterostructure at low temperature. The heterostructure with a twisted angle of 0° satisfies the angular momentum matching; the PL emission of interlayer excitons is more competitive than other quasi-particles at low temperature. The results help us confirm that the peak assignment for the interlayer excitons in heterostructure with a twisted angle of 0° in Figure 2g is reliable. In terms of the heterostructure with a twisted angle of 30°, similar to the case at room temperature, no obvious interlayer excitons are observed, and the luminescence intensity of WSe_2 also decreases with the decrease of temperature. While the PL peaks of negatively charged trions and neutral excitons in WS_2 are clearly separated and the binding energy of trions are approximately 40 meV. For 60° stacked heterostructure, negatively charged trions and neutral excitons in WS_2 still dominate the PL emission intensity as the temperature goes down. The luminescence intensity of WSe_2 is weaker than that of WS_2, but the positively charged trions and neutral excitons of WSe_2 are clearly separated. The interlayer excitons occupy a large proportion of PL emission at 77 K. Because the PL intensity of monolayer WSe_2 itself decreases with the decrease of temperature, the intralayer trions of WSe_2 occupy a disadvantage in competing with the interlayer excitons.

Based on previous analyses, the different optical behaviors of intralayer excitons, trions of heterostructures with different twisted angles mainly arise from (1) the charge transfer efficiency between two adjacent materials at different twisted angles being different, which makes the carrier concentration in the steady-state valley different; and (2) the formation rates of excitons and trions being different for heterostructures with different binding energies. To solve this puzzle, we used the femtosecond transient absorption spectrum (instrument response function ∼ 100 fs, see Figure S9) to obtain the formation rates of different particles[17,39−41] and calculated the carrier concentration according to the mass action model.[15] Here, the electron and hole transfers between WSe_2 and WS_2 are excited by a pump pulse where the central wavelength is 580 nm and the energy fluence is ∼1.9 μJ cm^{-2}. The corresponding differential reflection signals of monolayer WSe_2 are shown in Figure S10 for reference, where the rapid band renormalization is observed beacause the excitons quickly absorb excess holes preferentially form trions. The photon energy is above the band gaps of both WSe_2 and WS_2, it can induce electron and hole transfer as well as exciton transition in WSe_2 and WS_2. Excitons as well as trions of WSe_2 formed by hole transfer from WS_2 were monitored by measuring the differential reflection of a probe pulse, where the probe pulse was tuned to the *A* exciton and trion resonance of WSe_2, respectively, for different twisted angles of WS_2/WSe_2. The

DOI: 10.1021/acsphotonics.9b00855
ACS Photonics 2019, 6, 3082−3091

wavelength of the probe pulse can be obtained by the fitted PL peak, as shown in Figure 2g with pump fluence of 0.19 μJ cm^{-2}. The corresponding differential reflection signal ($\Delta R/R_0$) measured from WS_2/WSe_2 heterostructures with twisted angles of 0°, 30°, and 60° are shown in Figure 3d–f. As can be seen from the inset image of Figure 3d–f, the rising times of trions and excitons are quite different, which directly reflect the competion formation process in heterostructures with a twisted angle of 0°, 30°, and 60°. The corresponding schematics of exciton- and trion-related formation transitions between WS_2 and WSe_2 valleys at the K point in the Brillouin zone are shown in Figure 3a–c. ε_A and ε_A^+ represent binding energies of intralayer excitons and positive trions, respectively. For the heterostructure with a twisted angle of 0°, the rising time of trions and excitons are comparable, which means the time to form the trions and excitons is synchronized within ~1.5 ps after the excitation of pump laser. The formation processes of trions and excitons are synchronized in the heterostructure with a twisted angle of 0°. However, for excitons and trions of WSe_2 in the 30° twisted heterostructure, excitons are formed in preference to the trions after optical pumping. The excitons are quickly formed within ~1 ps and converted into trions after ~0.5 ps. As discussed above, the binding energies of trions are 31 and 52 meV, respectively, for heterostructures with twisted angles of 0° and 30°. The exciton to trion formation time decreases with the increase of trion binding energy, which is determined by the different Coulomb interaction in heterostructures with different twisted angles.[42] This explains why the formation time of trions for the 30° twisted angle is very short and the decay times of excitons and trions are comparable. For the 60° twisted angle heterostructure, as shown in Figure 3c, the binding energy reaches 80 meV, which means that the trion formation time should be smaller (<0.4 ps). As can be seen from the inset image of Figure 3f, the formation time of trions is significantly faster than that of the excitons. We can observe a small concave signal on the rising edge of the excitons and the time scales of trions and the concave signal are comparable as shown in Figure S11, which indicates that excitons tend to preferentially form trions first, and then form excitons after relaxation of trions is completed and the formation process of the trions affects the formation of excitons. This also explain why the PL emission ratios of interlayer excitons in 0° and 60° stacked heterostructure are different. Since not only the momentum match and stronger interlayer coupling give rise to a higher formation propability for interlayer excitons, but also the charge transfer induced intralayer trions will compete with the interlayer excitons and affect PL emission of the interlayer excitons from the K valley. For a 60° stacked heterostructure, the formation time of trions in WSe_2 is significantly faster than that of excitons; therefore, the excitons preferentially transformed into trions, owing to the less intralayer exciton binding energy compared to 0° stacked heterostructure.

The decay process of the signal can be well fitted by a biexponential function with two time constants τ_1 and τ_2 for heterostructures with twisted angles of 0° and 60°. However, a triexponential fitting curve with three time constants of τ_1, τ_2, and τ_3 is used for the heterostructure with a twisted angle of 30°, as given in Table 1. The decay process of the intralayer exciton signal of WSe_2 can be fitted as a fast decay time of τ_1 = 3 ps and a slow decay time of τ_2 = 34 ps, which agree well with a previous report.[19] Comparably, the decay time constants of the positive trions of WSe_2 are τ_1 = 2.3 ps and τ_2 = 20 ps,

Table 1

sample	type	A_1	τ_1 (ps)	A_2	τ_2 (ps)	A_3	τ_3 (ps)
0°	X	0.36	3.00	0.64	34.0		
	X^{T+}	0.19	2.30	0.81	20.0		
30°	X	0.87	0.23	0.06	5.0	0.07	77.0
	X^{T+}	0.93	0.20	0.03	2.2	0.04	23.0
60°	X	0.46	1.00	0.54	8.5		
	X^{T+}	0.97	0.20	0.03	3.7		

respectively. The fast decay (τ_1) of X_{WSe_2} is usually assigned to carrier–carrier scattering or the formation of trions with the excess hole.[43,42] The fast decay (τ_1) of $X^{T+}_{WSe_2}$ is associated with the thermal relaxation process. The slow decay times (τ_2) of both X_{WSe_2} and $X^{T+}_{WSe_2}$ are attributed to the carrier–phonon scattering time.[43,44] For the heterostructure with a twisted angle of 0°, the PL intensity is mainly dominated by intralayer excitons, and the trion formation time is ~3 ps, which is similar to that of the trion for thermal relaxation (~2.3 ps). In this situation, electrons and holes can be separated effectively by charge transfer, and momentum matching is satisfied in the 0° twisted heterostructure, which is more inclined to the formation of the interlayer exciton, as shown in Figure 3a. The fomation and transition rates of the trions and the intralayer excitons are comparable, and the intralayer excitons dominate the PL emission. For the decay process of 30° twisted heterostructure, a new fast decay channel occurs. In this scenario, both decay times of X_{WSe2} and X^{T}_{WSe2} exhibit an obvious reduction compared to that of the 0° twisted heterostructure. By fitting by a triexponential function, three time constants τ_1, τ_2, and τ_3 are obtained, respectively. The fast decay time (τ_1) of ~0.23 ps of X_{WSe2} gives it dominance (accounting for 87% of the emission), which is attributed to the ultrafast formation process of positive trions. The fast decay time (τ_1 = 0.2 ps) of $X^{T+}_{WSe_2}$ also gives it a similar dominance (accounting for 93% of emission), which is assigned to the thermal relaxation process. For the heterostructure with a twisted angle of 60°, the fast decay time (τ_1 = 0.2 ps) of $X^{T+}_{WSe_2}$ gives it a similar dominance (accounting for 97% of emission), which is assigned to the thermal transition process, but the fast decay time (τ_1 = 1 ps) of X_{WSe2} is similar to that of the heterostructure with a twisted angle of 0°, and this fast decay process occupies 46% of the total decay time. Hence, we assign the fast decay of τ_1 = 1 ps of X_{WSe2} to trapping of the excitons by surface trap states, and this also explains the significant difference between the relaxation time of the intralayer excitons and the trions for the 60° twisted angle. Here, the PL emission efficiency of the trions in heterostructure is both determined by the formation probability and formation time. In order to further confirm the reasons for the dominant PL efficiency in 30° and 60° heterostructures, we provide non-normalized differential reflection data, as shown in Figures S11and S12 to analyze the initial population of trions and excitons. The results prove that the different initial population of trions and excitons is not the main reason for the high PL efficiency of heterostructure with twisted angles of 0° and 60°.

We also calculated the steady state carrier concentration by using the mass action model to verify whether the charge transfer efficiencies between two adjacent materials are different with different twisted angles. The mass action law can be expressed as[45,46]

DOI: 10.1021/acsphotonics.9b00855
ACS Photonics 2019, 6, 3082–3091

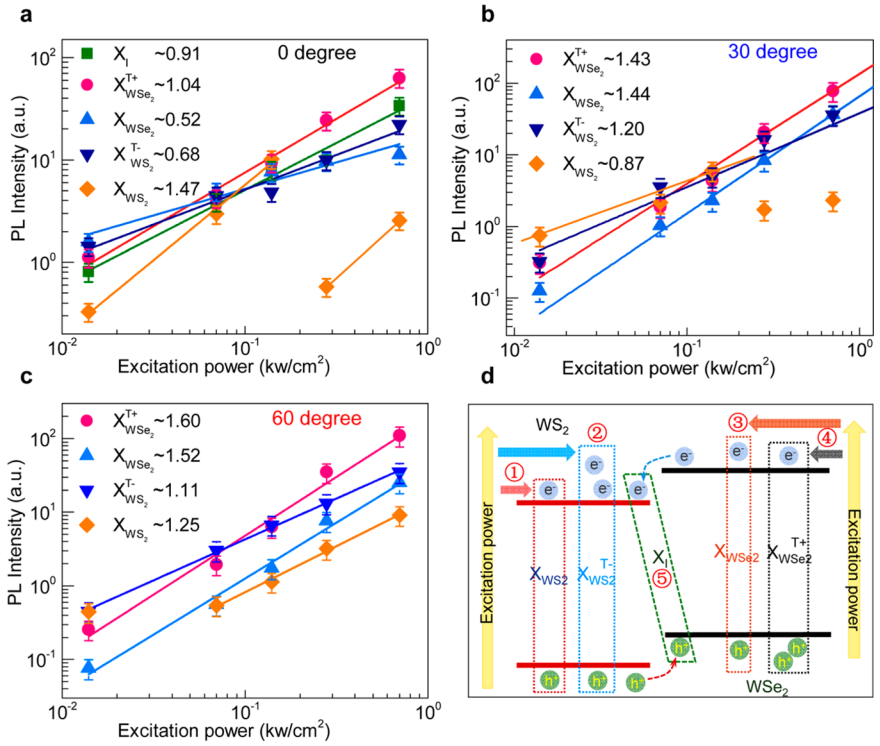

Figure 4. (a–c) Power-dependent PL integrated intensity spectrum of WS_2/WSe_2 heterostructure with twisted angles of 0°, 30°, and 60°, respectively. (d) Schematic diagram of the competition mechanism between quasi-particles in the heterostructure under different power conditions of excitation light, where (1)–(4) represent the direction of photogenerated carriers for emission of neutral excitons, negative trions in WS_2 and neutral excitons, and positive point trions in WSe_2, respectively.

$$\frac{N_A n_h}{N_{A^+}} = \frac{4 m_A m_h k_B T}{\pi \hbar^2 m_{A^+}} \exp\left(-\frac{E_{A^+}}{k_B T}\right) \quad (1)$$

$$\frac{I_{A^+}}{I_A} = \frac{\Gamma_{A^+}}{\Gamma_A} \cdot \frac{N_{A^+}}{N_A} \quad (2)$$

Here, $m_A = 0.79 m_0$, $m_A^+ = 1.25 m_0$, $m_h = 0.46\ m_0$, $m_e = 0.33 m_0$, and $k_B T = 25.9$ meV, respectively[8] (more details in Supporting Information, S12). As a result, the concentrations of holes in steady states of the heterostructure with twisted angles of 0°, 30°, and 60° are calculated to be $\sim 10^{12}$, $\sim 10^{13}$, and $\sim 10^{12}$ cm^{-2}, respectively. Through the calculation, we know that hole concentrations are within an order of magnitude in heterostructures with twisted angles of 0° and 60°, which means that carrier concentration is not the reason for the different ratios of trion luminescence. However, for heterostructure with twisted angle of 30°, a large concentration of carrier density is achieved by hole transfer from WS_2 to WSe_2, which leads to a large binding energy of trions in heterostructure. The results agree well with previous research by Katoch et al., and the giant renormalization of the spin–orbit splitting of the valence band in single-layer WS_2 attributed to the formation of trionic quasi-particles has been directly observed upon electron doping by using microfocused angle-resolved photoemission spectroscopy (microARPES).[47] Therefore, the increased trion luminescence ratio in 30° twisted heterostructure is caused by the higher carrier concentration, which leads to the accumulation of a large number of residual carriers for the formation of trions. As for the interlayer excitons, it does not satisfy the momentum matching condition, so most of the transferred holes are used to form intralayer trions. However, for the heterostructure with a twisted angle of 60°, the large proportion of trion luminescence is due to the fact that the formation rate for trions is significantly faster than that of excitons.

After confirming the formation rates and steady state carrier concentration of excitons and trions in heterostructures with different twisted angles, we discussed about the inclination of photogenerated carriers to form different quasi-particles by analyzing the slope of power-dependent PL spectrum, as shown in Figure S4a–c. Figure 4a–c shows plots of the corresponding integrated PL intensity (I) versus laser intensity (L) on a log–log scale where the excitation wavelength is fixed at 514 nm. The power dependence curve can be described by an $I \sim L^k$ law, where k is a coefficient. According to previous research, the coefficient k can be used to reflect the origin of different features and the value is generally in the range $1 < k < 2$ for free- and bound-exciton emission, whereas $k < 1$ for free-to-bound and donor–acceptor pair recombination.[48] For the complex heterostructure system, the value of k mainly reflected the competing inclination of photogenerated carriers to form different quasi-particles: (1) forming excitons in WS_2, (2) replenishing electrons to form trions in WS_2, (3) forming excitons in WSe_2, (4) supplying electrons to form trions in WSe_2, and (5) forming interlayer excitons. For the heterostructure with a 0° twisted angle, trions in WSe_2 and interlayer excitons nearly follow a linear relationship with excitation power, which indicates an exciton-like transition for processes (4) and (5); k values of X_{WSe2} and X^{T-}_{WS2} are in the range of 0 to 1, exhibiting a sublinear relationship (for (2) and (3)) between PL intensity and excitation power which means the formation of excitons of WSe_2 and trions of WS_2 occupy a disadvantage in the competition process. For the 30° twisted angle, processes (3) and (4) in WSe_2 are more competitive

DOI: 10.1021/acsphotonics.9b00855
ACS Photonics 2019, 6, 3082–3091

compared to processes (1) and (2) in WS_2 but the k value for all of them satisfy the relationship $1 < k < 2$. These k values are consistent with the results of PL spectra for the 30° twisted angle. Although trion components in WSe_2 begin to dominate, both the intralayer exciton X_{WSe2} and the trion X^{T+}_{WSe2} are both likely to follow a radiative transition process. Meanwhile, the proportion of luminescence of WSe_2 began to rise, showing a competitive trend with WS_2. In terms of the competition process in a heterostructure with a twisted angle of 60°, the photonic carriers are more inclined to form intralayer excitons X_{WSe2} and trions X^{T+}_{WSe2} in processes (3) and (4) and exhibit a dominant trend, which explains the optical behaviors for the 60° twisted angle.

All the results helped us to understand the formation difficulty of various quasi-particles in heterostructures and the distinct competition behaviors are mainly caused by the change of Coulomb interaction. As the twisted angle of the heterostructure is different, the binding energy of trions changes significantly ranging from (30−80 meV), which leads to the change of the coulomb interaction strength. In the power-dependent PL spectrum, the emergence of sublinear and superlinear relations and transformation between them directly reflect the way that "many-body" effect affects the competition process among quasi-particles in heterostructures with different twisted angles. These results clearly reveal the selection tendency of different quasi-particles formed by photogenerated carriers in different twisted heterostructures, which lays a theoretical foundation for our future research on heterostructure optoelectronic properties.

CONCLUSION

In summary, we provided further understanding of twisted-angle-dependent optical behaviors of intralayer excitons and trions in WS_2/WSe_2 heterostructure with respect to the competition mechanism of intralayer excitons and trions. The mass action model and the formation dynamics confirmed that the increased luminescence ratio of trions in the heterostructure with twisted angle of 30° and 60° are caused, respectively, by the higher formation probability and faster formation rate compared to excitons. Power-dependent PL spectra reveal the way that "many-body" influence the formation probability of excitons and trions in the heterostructure. All the results help us to understand the optical behaviors of intralayer excitons and trions in twisted angle-dependent heterostructures. It is critically important for evaluating and improving the performance of two-dimensional materials based optoelectronic devices.

EXPERIMENTAL SECTION

Sample Preparation. Monolayers WS_2 and WSe_2 were grown on c-plane sapphire substrate separately by low pressure chemical vapor deposition (LPCVD) methods in a two-temperature-zone horizontal tube furnace. WO_3 powders in a quartz boat were positioned at the center of the first zone; while the sapphire substrate was placed at the second zone about 5 cm from the WO_3 powders. Sulfur or selenium powders were placed upstream of first zone 15 and 10 cm from the WO_3 powders, respectively. During the growth of WS_2, both zones were heated to 887 °C within 35 min and maintained the temperature for 70 min. Sulfur powders were heated to 90 °C by a heating tape. A mixture of 80 sccm Ar and 10 sccm H_2 was induced into the tube furnace as a carrier gas. The pressure was maintained at 100 Pa. For the growth of WSe_2, the first and second zones were heated to 950 and 800 °C within 50 min and were maintained for 30 min to grow monolayer WSe_2. The carrier gas was a mixture of 50 sccm Ar and 25 sccm H_2. The pressure was maintained at 80 Pa.

WS_2/WSe_2 Heterostructure. WS_2/WSe_2 heterostructure was prepared by a PMMA-assisted transfer method. Here, WS_2 flakes grown on sapphire were covered with PMMA (AR-P 679.04) by spin coating. After 15 min of heating at 100 °C, the PMMA/WS_2 structure was separated from the sapphire substrate through the etching of a 30% KOH solution (100 °C and 0.5−1.0 h) and then they are soaked in DI water to clean the KOH residue. Afterward, the PMMA/WS_2 was transferred onto monolayer WSe_2 grown on a sapphire substrate and heated on a hot plate at 100 °C for about 10 min. After that, the PMMA/WS_2/WSe_2 structure was peeled off the sapphire substrate and transferred onto the SiO_2/Si substrate by the same way described above. Then, the PMMA layer was removed by immersing the samples into acetone. Finally, to remove the polymer residue, the transferred WS_2/WSe_2 samples were annealed at 350 °C in a Ar/H_2 flow (50/20 sccm, 60 Pa) for 3 h.

Optical Characterizations. Steady-state PL spectroscopy was carried out by using Renishaw Spectrometer System, a CW laser with wavelength of 514 nm was focused onto an WS_2/WSe_2 heterstructure through an objective (Leica, 100×/NA 0.95) with size of 250 nm. For transient absorption spectroscopy setup, the large part of 800 nm output (80%) from the Ti:sapphire oscillator (∼100 fs, 76 MHz) was used to serve as pump pulse for the OPO and the rest acted as the probe pulse. The output from OPO was the pump beam with a wavelength fixed at 580 nm. Both pump and probe beams were focused on the sample through a 20×, 0.42 numerical aperture (NA) objectives, and were spatially overlapped at the sample. The signals were collected by the same objective, and the probe signal was detected with an avalanche photodiode (APD110A2/M, Thorlabs).

ASSOCIATED CONTENT

Supporting Information

The Supporting Information is available free of charge at https://pubs.acs.org/doi/10.1021/acsphotonics.9b00855.

Power-dependent and temperature-dependent PL spectra. SHG spectra. Band structure of heterostructures. Peak position versus excitation power. The instrument response function (IRF) for transient absorption. Differential reflection signal. Carrier concentration calculated by the mass action model (PDF)

AUTHOR INFORMATION

Corresponding Authors

*E-mail: liuxf@nanoctr.cn.
*E-mail: q_zhang@pku.edu.cn.
*E-mail: shenchao@semi.ac.cn.

ORCID

Zhepeng Zhang: 0000-0002-9870-0720
Jun Zhang: 0000-0002-9831-6796
Lijun Zhang: 0000-0002-6438-5486
Jiong Lu: 0000-0002-3690-8235
Chao Shen: 0000-0002-3664-4874
Yanfeng Zhang: 0000-0003-1319-3270

DOI: 10.1021/acsphotonics.9b00855
ACS Photonics 2019, 6, 3082−3091

Qing Zhang: 0000-0002-6869-0381
Xinfeng Liu: 0000-0002-7662-7171

Author Contributions

#These authors contributed equally to this work.

Notes

The authors declare no competing financial interest.

■ ACKNOWLEDGMENTS

X.F.L. thanks the support from the Ministry of Science and Technology (2017YFA0205004 and 2016YFA0200700), National Natural Science Foundation of China (Nos. 21673054 and 11874130), Beijing Municipal Natural Science Foundation (4182076 and 4184109) and Open Research Fund Program of the State Key Laboratory of Low-Dimensional Quantum physics (KF201902). C.S. acknowledges the support from the NSFC Grant No. 11404324. Y.F.Z. thanks the support from the National Natural Science Foundation of China (No. 51861135201).

■ REFERENCES

(1) Geim, A. K.; Grigorieva, I. V. Van Der Waals Heterostructures. *Nature* **2013**, *499*, 419.
(2) Novoselov, K. S.; Mishchenko, A.; Carvalho, A.; Castro Neto, A. H. 2D Materials and Van Der Waals Heterostructures. *Science* **2016**, *353*, 9439.
(3) Raja, A.; Chaves, A.; Yu, J.; Arefe, G.; Hill, H. M.; Rigosi, A. F.; Berkelbach, T. C.; Nagler, P.; Schüller, C.; Korn, T.; Nuckolls, C.; Hone, J.; Brus, L. E.; Heinz, T. F.; Reichman, D. R.; Chernikov, A. Coulomb Engineering of the Bandgap and Excitons in Two-Dimensional Materials. *Nat. Commun.* **2017**, *8*, 15251.
(4) Mak, K. F.; He, K.; Lee, C.; Lee, G. H.; Hone, J.; Heinz, T. F.; Shan, J. Tightly Bound Trions in Monolayer MoS_2. *Nat. Mater.* **2013**, *12*, 207.
(5) Courtade, E.; Semina, M.; Manca, M.; Glazov, M. M.; Robert, C.; Cadiz, F.; Wang, G.; Taniguchi, T.; Watanabe, K.; Pierre, M.; Escoffier, W.; Ivchenko, E. L.; Renucci, P.; Marie, X.; Amand, T.; Urbaszek, B. Charged Excitons in Monolayer WSe_2: Experiment and Theory. *Phys. Rev. B: Condens. Matter Mater. Phys.* **2017**, *96*, 085302.
(6) Heo, H.; Sung, J. H.; Cha, S.; Jang, B. G.; Kim, J. Y.; Jin, G.; Lee, D.; Ahn, J. H.; Lee, M. J.; Shim, J. H.; Choi, H.; Jo, M. H. Interlayer Orientation-Dependent Light Absorption and Emission in Monolayer Semiconductor Stacks. *Nat. Commun.* **2015**, *6*, 7372.
(7) Shiue, R.-J.; Efetov, D. K.; Grosso, G.; Peng, C.; Fong, K. C.; Englund, D. Active 2D Materials for on-Chip Nanophotonics and Quantum Optics. *Nanophotonics* **2017**, *6*, 1329.
(8) Jadczak, J.; Kutrowska-Girzycka, J.; Kapuscinski, P.; Huang, Y. S.; Wojs, A.; Bryja, L. Probing of Free and Localized Excitons and Trions in Atomically Thin WSe_2, WS_2, $MoSe_2$ and MoS_2 in Photoluminescence and Reflectivity Experiments. *Nanotechnology* **2017**, *28*, 395702.
(9) Schaibley, J. R.; Yu, H.; Clark, G.; Rivera, P.; Ross, J. S.; Seyler, K. L.; Yao, W.; Xu, X. Valleytronics in 2D Materials. *Nat. Rev. Mater.* **2016**, *1*, 16055.
(10) Rivera, P.; Seyler, K. L.; Yu, H.; Schaibley, J. R.; Yan, J.; Mandrus, D. G.; Yao, W.; Xu, X. Valley-Polarized Exciton Dynamics in a 2D Semiconductor Heterostructure. *Science* **2016**, *351*, 688.
(11) Jariwala, D.; Sangwan, V. K.; Lauhon, L. J.; Marks, T. J.; Hersam, M. C. Emerging Device Applications for Semiconducting Two-Dimensional Transition Metal Dichalcogenides. *ACS Nano* **2014**, *8*, 1102.
(12) Hao, K.; Xu, L.; Nagler, P.; Singh, A.; Tran, K.; Dass, C. K.; Schuller, C.; Korn, T.; Li, X.; Moody, G. Coherent and Incoherent Coupling Dynamics between Neutral and Charged Excitons in Monolayer $MoSe_2$. *Nano Lett.* **2016**, *16*, 5109.
(13) Jiang, S.; Shan, J.; Mak, K. F. Electric-Field Switching of Two-Dimensional Van Der Waals Magnets. *Nat. Mater.* **2018**, *17*, 406.
(14) Ross, J. S.; Wu, S.; Yu, H.; Ghimire, N. J.; Jones, A. M.; Aivazian, G.; Yan, J.; Mandrus, D. G.; Xiao, D.; Yao, W.; Xu, X. Electrical Control of Neutral and Charged Excitons in a Monolayer Semiconductor. *Nat. Commun.* **2013**, *4*, 1474.
(15) Lin, Y.; Ling, X.; Yu, L.; Huang, S.; Hsu, A. L.; Lee, Y. H.; Kong, J.; Dresselhaus, M. S.; Palacios, T. Dielectric Screening of Excitons and Trions in Single-Layer MoS_2. *Nano Lett.* **2014**, *14*, 5569.
(16) Drüppel, M.; Deilmann, T.; Krüger, P.; Rohlfing, M. Diversity of Trion States and Substrate Effects in the Optical Properties of an MoS_2 Monolayer. *Nat. Commun.* **2017**, *8*, 2117.
(17) Gao, S.; Liang, Y.; Spataru, C. D.; Yang, L. Dynamical Excitonic Effects in Doped Two-Dimensional Semiconductors. *Nano Lett.* **2016**, *16*, 5568.
(18) Mouri, S.; Miyauchi, Y.; Matsuda, K. Tunable Photoluminescence of Monolayer MoS_2 Via Chemical Doping. *Nano Lett.* **2013**, *13*, 5944.
(19) Wang, K.; Huang, B.; Tian, M.; Ceballos, F.; Lin, M. W.; Mahjouri-Samani, M.; Boulesbaa, A.; Puretzky, A. A.; Rouleau, C. M.; Yoon, M.; Zhao, H.; Xiao, K.; Duscher, G.; Geohegan, D. B. Interlayer Coupling in Twisted WSe_2/WS_2 Bilayer Heterostructures Revealed by Optical Spectroscopy. *ACS Nano* **2016**, *10*, 6612.
(20) Calman, E. V.; Fogler, M. M.; Butov, L. V.; Hu, S.; Mishchenko, A.; Geim, A. K. Indirect Excitons in Van Der Waals Heterostructures at Room Temperature. *Nat. Commun.* **2018**, *9*, 1895.
(21) Deilmann, T.; Thygesen, K. S. Interlayer Trions in the MoS_2/WS_2 Van Der Waals Heterostructure. *Nano Lett.* **2018**, *18*, 1460.
(22) Hu, X.; Kou, L.; Sun, L. Stacking Orders Induced Direct Band Gap in Bilayer $MoSe_2$-WSe_2 Lateral Heterostructures. *Sci. Rep.* **2016**, *6*, 31122.
(23) Torun, E.; Miranda, H. P. C.; Molina-Sánchez, A.; Wirtz, L. Interlayer and Intralayer Excitons in MoS_2/WS_2 and $MoSe_2/WSe_2$ Heterobilayers. *Phys. Rev. B: Condens. Matter Mater. Phys.* **2018**, *97*, 245427.
(24) Choi, C.; Huang, J.; Cheng, H.-C.; Kim, H.; Vinod, A. K.; Bae, S.-H.; Özçelik, V. O.; Grassi, R.; Chae, J.; Huang, S.-W.; Duan, X.; Kaasbjerg, K.; Low, T.; Wong, C. W. Enhanced Interlayer Neutral Excitons and Trions in Trilayer Van Der Waals Heterostructures. *npj 2D Mater. Appl.* **2018**, *2*, 30.
(25) Zhang, C.; Chuu, C.-P.; Ren, X.; Li, M.-Y.; Li, L.-J.; Jin, C.; Chou, M.-Y.; Shih, C.-K. Interlayer Couplings, Moiré Patterns, and 2D Electronic Superlattices in MoS_2/WSe_2 Hetero-Bilayers. *Sci. Adv.* **2017**, *3*, 1601459.
(26) Jin, C.; Regan, E. C.; Yan, A.; Iqbal Bakti Utama, M.; Wang, D.; Zhao, S.; Qin, Y.; Yang, S.; Zheng, Z.; Shi, S.; Watanabe, K.; Taniguchi, T.; Tongay, S.; Zettl, A.; Wang, F. Observation of Moiré Excitons in WSe_2/WS_2 Heterostructure Superlattices. *Nature* **2019**, *567*, 76.
(27) Seyler, K. L.; Rivera, P.; Yu, H.; Wilson, N. P.; Ray, E. L.; Mandrus, D. G.; Yan, J.; Yao, W.; Xu, X. Signatures of Moiré-Trapped Valley Excitons in $MoSe_2/WSe_2$ Heterobilayers. *Nature* **2019**, *567*, 66.
(28) Tran, K.; Moody, G.; Wu, F.; Lu, X.; Choi, J.; Kim, K.; Rai, A.; Sanchez, D. A.; Quan, J.; Singh, A.; Embley, J.; Zepeda, A.; Campbell, M.; Autry, T.; Taniguchi, T.; Watanabe, K.; Lu, N.; Banerjee, S. K.; Silverman, K. L.; Kim, S.; Tutuc, E.; Yang, L.; MacDonald, A. H.; Li, X. Evidence for Moiré Excitons in Van Der Waals Heterostructures. *Nature* **2019**, *567*, 71.
(29) Kunstmann, J.; Mooshammer, F.; Nagler, P.; Chaves, A.; Stein, F.; Paradiso, N.; Plechinger, G.; Strunk, C.; Schüller, C.; Seifert, G.; Reichman, D. R.; Korn, T. Momentum-Space Indirect Interlayer Excitons in Transition-Metal Dichalcogenide Van Der Waals Heterostructures. *Nat. Phys.* **2018**, *14*, 801.
(30) Chakraborty, C.; Goodfellow, K. M.; Nick Vamivakas, A. Localized Emission from Defects in $MoSe_2$ Layers. *Opt. Mater. Express* **2016**, *6*, 2081.
(31) Shang, J.; Shen, X.; Cong, C.; Peimyoo, N.; Cao, B.; Eginligil, M.; Yu, T. Observation of Excitonic Fine Structure in a 2D Transition-Metal Dichalcogenide Semiconductor. *ACS Nano* **2015**, *9*, 647.

DOI: 10.1021/acsphotonics.9b00855
ACS Photonics 2019, 6, 3082−3091

(32) Kim, C.-J.; Brown, L.; Graham, M. W.; Hovden, R.; Havener, R. W.; McEuen, P. L.; Muller, D. A.; Park, J. Stacking Order Dependent Second Harmonic Generation and Topological Defects in H-BN Bilayers. *Nano Lett.* **2013**, *13*, 5660.
(33) Li, Y.; Rao, Y.; Mak, K. F.; You, Y.; Wang, S.; Dean, C. R.; Heinz, T. F. Probing Symmetry Properties of Few-Layer MoS_2 and H-BN by Optical Second-Harmonic Generation. *Nano Lett.* **2013**, *13*, 3329.
(34) Mishina, E.; Sherstyuk, N.; Lavrov, S.; Sigov, A.; Mitioglu, A.; Anghel, S.; Kulyuk, L. Observation of Two Polytypes of MoS_2 Ultrathin Layers Studied by Second Harmonic Generation Microscopy and Photoluminescence. *Appl. Phys. Lett.* **2015**, *106*, 131901.
(35) Shi, J.; Yu, P.; Liu, F.; He, P.; Wang, R.; Qin, L.; Zhou, J.; Li, X.; Zhou, J.; Sui, X.; Zhang, S.; Zhang, Y.; Zhang, Q.; Sum, T. C.; Qiu, X.; Liu, Z.; Liu, X. 3R Mos_2 with Broken Inversion Symmetry: A Promising Ultrathin Nonlinear Optical Device. *Adv. Mater.* **2017**, *29*, 1701486.
(36) Jiang, T.; Liu, H.; Huang, D.; Zhang, S.; Li, Y.; Gong, X.; Shen, Y.-R.; Liu, W.-T.; Wu, S. Valley and Band Structure Engineering of Folded MoS_2 Bilayers. *Nat. Nanotechnol.* **2014**, *9*, 825.
(37) Zhu, B.; Chen, X.; Cui, X. Exciton Binding Energy of Monolayer WS_2. *Sci. Rep.* **2015**, *5*, 9218.
(38) Bellus, M. Z.; Ceballos, F.; Chiu, H.-Y.; Zhao, H. Tightly Bound Trions in Transition Metal Dichalcogenide Heterostructures. *ACS Nano* **2015**, *9*, 6459.
(39) Chen, H.; Wen, X.; Zhang, J.; Wu, T.; Gong, Y.; Zhang, X.; Yuan, J.; Yi, C.; Lou, J.; Ajayan, P. M.; Zhuang, W.; Zhang, G.; Zheng, J. Ultrafast Formation of Interlayer Hot Excitons in Atomically Thin MoS_2/WS_2 Heterostructures. *Nat. Commun.* **2016**, *7*, 12512.
(40) Huang, J.; Hoang, T. B.; Mikkelsen, M. H. Probing the Origin of Excitonic States in Monolayer WSe_2. *Sci. Rep.* **2016**, *6*, 22414.
(41) Wen, X.; Chen, H.; Wu, T.; Yu, Z.; Yang, Q.; Deng, J.; Liu, Z.; Guo, X.; Guan, J.; Zhang, X.; Gong, Y.; Yuan, J.; Zhang, Z.; Yi, C.; Guo, X.; Ajayan, P. M.; Zhuang, W.; Liu, Z.; Lou, J.; Zheng, J. Ultrafast Probes of Electron-Hole Transitions between Two Atomic Layers. *Nat. Commun.* **2018**, *9*, 1859.
(42) Singh, A.; Moody, G.; Tran, K.; Scott, M. E.; Overbeck, V.; Berghäuser, G.; Schaibley, J.; Seifert, E. J.; Pleskot, D.; Gabor, N. M.; Yan, J.; Mandrus, D. G.; Richter, M.; Malic, E.; Xu, X.; Li, X. Trion Formation Dynamics in Monolayer Transition Metal Dichalcogenides. *Phys. Rev. B: Condens. Matter Mater. Phys.* **2016**, *93*, 041401.
(43) Shi, H.; Yan, R.; Bertolazzi, S.; Brivio, J.; Gao, B.; Kis, A.; Jena, D.; Xing, H. G.; Huang, L. Exciton Dynamics in Suspended Monolayer and Few-Layer MoS_2 2D Crystals. *ACS Nano* **2013**, *7*, 1072.
(44) Titze, M.; Li, B.; Zhang, X.; Ajayan, P. M.; Li, H. Intrinsic Coherence Time of Trions in Monolayer $MoSe_2$ Measured Via Two-Dimensional Coherent Spectroscopy. *Phys. Rev. Mater.* **2018**, *2*, 054001.
(45) Lin, Y.; Ling, X.; Yu, L.; Huang, S.; Hsu, A. L.; Lee, Y.-H.; Kong, J.; Dresselhaus, M. S.; Palacios, T. Dielectric Screening of Excitons and Trions in Single-Layer MoS_2. *Nano Lett.* **2014**, *14*, 5569.
(46) Zhang, Q.; Naylor, C. H.; Gao, Z.; Wu, R.; Abidi, I. H.; Zhao, M. Q.; Ding, Y.; Cagang, A. A.; Zhuang, M.; Ou, X.; Luo, Z. Recoil Effect and Photoemission Splitting of Trions in Monolayer MoS_2. *ACS Nano* **2017**, *11*, 10808.
(47) Katoch, J.; Ulstrup, S.; Koch, R. J.; Moser, S.; McCreary, K. M.; Singh, S.; Xu, J.; Jonker, B. T.; Kawakami, R. K.; Bostwick, A.; Rotenberg, E.; Jozwiak, C. Giant Spin-Splitting and Gap Renormalization Driven by Trions in Single-Layer WS_2/H-BN Heterostructures. *Nat. Phys.* **2018**, *14*, 355.
(48) Schmidt, T.; Lischka, K.; Zulehner, W. Excitation-Power Dependence of the near-Band-Edge Photoluminescence of Semiconductors. *Phys. Rev. B: Condens. Matter Mater. Phys.* **1992**, *45*, 8989.

DOI: 10.1021/acsphotonics.9b00855
ACS Photonics 2019, 6, 3082−3091